Electronic Supplementary Material (ESI) for Chemical Science.

Supporting Information

Towards an object-oriented design of active hydrogen evolution catalysts on single-atom alloys

Chuan Zhou,[a] Jia Yue Zhao,[b] Peng Fei Liu,[b] Jianfu Chen,[a] Sheng Dai,[c] Hua Gui Yang,[b] P. Hu,[ad] and Haifeng Wang[a,*]

[a]Key Laboratory for Advanced Materials, Research Institute of Industrial Catalysis and Centre for Computational Chemistry, East China University of Science and Technology, Shanghai 200237, China

[b]Key Laboratory for Ultrafine Materials of Ministry of Education, Shanghai Engineering Research Center of Hierarchical Nanomaterials, School of Materials Science and Engineering, East China University of Science and Technology, 130 Meilong Road, Shanghai 200237, China.

[c]Key Laboratory for Advanced Materials and Feringa Nobel Prize Scientist Joint Research Center, Institute of Fine Chemicals, School of Chemistry and Molecular Engineering, East China University of Science and Technology, 130 Meilong Road, Shanghai 200237, China.

[d]School of Chemistry and Chemical Engineering, The Queen’s University of Belfast, Belfast BT9 5AG, U.K.

Note S1: Theoretical methods

Genetic algorithm and encoding. Genetic-algorithm-based (GA) global optimization method can assist in catalyst design using crossover and mutation (see Fig. 1 in main text), the potential catalytic materials that close to the criteria are gradually found after continuous iteration in this process. Herein, we independently completed the construction of the whole automated workflow. Specifically, we compiled the GA process according to the genetic principle, and customize some advanced functions, such as doping operator. Some underlying functions in the python packages Pymatgen[1] and ASE[2] were used. Additionally, Portable Batch System (PBS) as the queuing system is integrated into our workflow to fulfill job submission and scheduling. Notably, encoding the surface structure is one of the key step for the algorithm. For 9 host metals, we use numbers 1 to 9 to represent them, respectively. {1: 'Ag', 2: 'Al', 3: 'Au', 4: 'Cu', 5: 'Ir', 6: 'Ni', 7: 'Pd', 8: 'Pt', 9: 'Rh'}. Likewise, for 29 guest metals, we use numbers 1 to 29 to represent them, respectively. {1: 'Al', 2: 'Si', 3: 'Ti', 4: 'V', 5: 'Cr', 6: 'Mn', 7: 'Fe', 8: 'Co', 9: 'Ni', 10: 'Cu', 11: 'Zn', 12: 'Ga', 13: 'Ge', 14: 'As', 15: 'Mo', 16: 'Ru', 17: 'Rh', 18: 'Pd', 19: 'Ag', 20: 'In', 21: 'Sn', 22: 'Sb', 23: 'W', 24: 'Re', 25: 'Os', 26: 'Ir', 27: 'Pt', 28: 'Au', 29: 'Pb'}. A specific structure can be mapped to a structural-gene-represented string. For example, Pd-Fe-Au configuration indicates the Pd host metal with Fe and Au single atom that replace two Pd atoms of surface, its encoding is expressed as [7, 7, 16], and the next crossover and mutation operations are applied to the coding. In addition, the fitness function determines the convergence speed of GA and whether it can find the optimal solution, which is defined as follows:

$$\text{fitness}(x)=1/|E_x-E_0| \qquad \text{(S1)}$$

where E_x and E_0 represent the individual adsorption energy of hydrogen and the target adsorption energy of hydrogen, respectively. In this work, GA used by us had a population size of 10 with 20 generations. The crossover employed two single points with the probability of crossover being 0.8, indicating 80% of the strings were picked up randomly in a given generation for crossover. Mutation probability was kept at 0.2.

Computational details. All the DFT calculations were performed with the Perdew−Burke−Ernzerhof (PBE) functional using the VASP code[3-4]. The project-augmented wave (PAW) method was applied to represent the core-valence electron interaction. The valence electronic states were expanded in plane wave basis sets with energy cutoff at 400 eV. The fcc(111) surfaces most exposed by nine host metal (Ag, Al, Au, Cu, Ir, Ni, Pd, Pt and Rh) were modeled as a p(3×3) periodic slab with four layers for the adsorption of hydrogen, The bottom two layers are fixed, and all other atoms are fully relaxed. 3×3×1 k-point mesh was used for these surface slabs. For the bulk structure, 5×5×5 k-point mesh was used. All the vacuum between slabs is 10 Å. The force threshold for the optimization was 0.05 eV/Å. In this work, the hydrogen adsorption energy (E_H) was calculated by using the following equation:

$$E_H = E(H/SAAs) - E(SAAs) - 1/2E(H_2) \qquad \text{(S2)}$$

where $E(H/SAAs)$ is the total energy of the interacting H/SAAs system, $E(SAAs)$ and $E(H_2)$ are the total energies of the gas-phase H_2 molecule and the SAAs. With this definition, a more negative value of adsorption energy suggests the stronger adsorption.

Code availability. The code used to perform this work is available at https://www.catkinas.com/downloads.

Note S2: Experimental methods

Chemicals. Nickel(II) chloride hexahydrate ($NiCl_2 \cdot 6H_2O$) and sodium molybdate dihydrate ($Na_2MoO_4 \cdot 2H_2O$) were purchased from Sinopharm Chemical Reagent Co. Ltd. Aluminum nitrate nonahydrate ($Al(NO_3)_3 \cdot 9H_2O$), gallium nitrate hydrate ($Ga(NO_3)_3 \cdot xH_2O$) and urea ($CO(NH_2)_2$) were purchased from Shanghai Aladdin Biochemical Technology Co. Ltd. Indium nitrate hydrate ($InN_3O_9 \cdot xH_2O$) was purchased from Shanghai Macklin Biochemical Co. Ltd. Ethanol was purchased from Shanghai Titan Scientific Co. Ltd. All reagents were analytical grade and used without any further purification. Deionized (DI) water used in our experiments was supplied by Milli-Q System (Millipore, Billerica, MA).

The pre-treatment of Ni foam. Typically, a commercial nickel foam (NF, 1.6-mm thickness, 110 p.p.i., geometric area of 1 cm^2 for performance evaluation) was sonicated with acetone and ethanol for 15 min, respectively. Then, the NF was put into a 3.0 mol L^{-1} HCl solution for 15 min to clean the surface oxide layer. After that, the NF was washed with water and ethanol for several times and dried in a vacuum oven for the further use.

The synthesis of NiAl, NiGa and NiIn bimetallic precursors. The NiAl, NiGa and NiIn precursor were synthesized through a hydrothermal method. In a typical synthesis of NiAl precursor, 1 mmol $NiCl_2·6H_2O$, 1 mmol $Al(NO_3)_3·9H_2O$ and 10 mmol urea were dissolved in a Teflon autoclave containing 20 mL H_2O to form a transparent solution. Then one piece of pre-treated NF was immersed into the above solution. After continuous sonicating for 5 min, the autoclave was put into an oven and heated at 160 ℃ for 6 h. After that the autoclave was cooling down to room temperature, the NiAl precursor was taken out and washed with deionized water and ethanol for several times before transferred into the vacuum oven. The synthesis of NiGa and NiIn precursors were similar to the process of NiAl precursor, except the metal nitrate precursors were replaced by $Ga(NO_3)_3·xH_2O$ or $In(NO_3)_3·xH_2O$. For the Ni_3Al precursor sample, $NiCl_2·6H_2O$ (1 mmol) and $Al(NO_3)_3·9H_2O$ (0.33 mmol) were dissolved in H_2O (20 mL) in a autoclave, and the remainder of the procedure was the same.

The synthesis of NiAl, NiGa and NiIn bimetallic electrocatalysts. For the preparation of bimetallic alloys, the above synthesized bimetallic precursors were transferred into a ceramic boat and placed in a tube furnace. The sample was heated to 550 ℃ with a heating rate of 5 ℃ min^{-1} and kept at 550 ℃ for 2 h under hydrogen gas (40 sccm) before cooling down to room temperature naturally. After that, the synthesized electrocatalysts were ready for electrochemical tests. Notes: The freshly prepared electrocatalysts would be easily oxidized in the air.

The preparation of NiMo bimetallic electrocatalyst. The synthesis of NiMo alloy was based on the modified method[5-7]. Typically, a pre-treated NF was immersed into 20 mL of H_2O containing 1 mmol of $NiCl_2 \cdot 6H_2O$ and 1 mmol Na_2MoO_4 in a Teflon autoclave. After continuous sonicating for 5 min, the autoclave was put into an oven and heated at 160 ℃ for 6 h. After that the autoclave was cooling down to room temperature, the NiMo alloy precursor was taken out and washed with deionized water and ethanol for several times before drying. Then the NF was transferred into a ceramic boat and placed in a tube furnace. The sample was heated to 550 ℃ with a heating rate of 5 ℃ min^{-1} and kept at 550 ℃ for 2 h under hydrogen gas (40 sccm) before cooling down to room temperature naturally. Notes: The NiMo-based precursor (*e.g.*, $NiMoO_4$) before H_2 treatment would not be completely reduced with existence of NiMo alloy and $NiMo_4$ in the obtained sample, which were coincident to the reported references[5-7].

Characterizations. The crystal structure of the samples was examined by X-ray diffraction (XRD, D/max2550V). Scanning transmission electron microscopy (STEM) characterization was performed using ThermoFisher Talos F200X. High angle annular dark field (HAADF)-STEM images were recorded using a convergence semi angle of 11 mrad, and inner- and outer collection angles of 59 and 200 mrad, respectively. Energy dispersive X-ray spectroscopy (EDS) was carried out using 4 in-column Super-X detectors.

Electrochemical measurements. The NiAl, Ni_3Al, NiGa, NiIn and NiMo on the NF were directly used as the working electrodes for electrochemical tests. All electrochemical studies were performed using an electrochemical station (CHI 760E) in a three-electrode compartment with modified Ni foam as the working electrode, a Ag/AgCl/3.5 M KCl electrode as the reference electrode and a graphite rod as the counter electrode. The Ag/AgCl/3.5 M KCl reference electrode was calibrated with respect to RHE. The calibration was performed in the high-purity H_2 saturated electrolyte with Pt mesh as the working electrode and counter electrode. CVs were run at a scan rate of 1 mV s^{-1}, and the average of the two potentials at which the current crossed zero was taken to be the thermodynamic potential for the hydrogen electrode reactions (1.001 V in the 1.0 M KOH, Fig. S4). The electrocatalytic activities towards HER were examined by polarization curves with a scan rate of 2 mV s^{-1} in H_2-saturated 1.0 M KOH solution at ambient temperature. All potentials were referenced to reversible hydrogen electrode (RHE) by following calculations: $E_{RHE} = E_{Ag/AgCl} + 1.001$ V. All LSV curves were corrected with *iR*-compensation (90%) while the equivalent series resistance (Rs) can be obtained through the *iR*-compensation test before the test. For the stability tests, a Ni foam decorated with NiMo-based electrocatalyst was used as working electrode and the chronopotentiometric curve was conducted at the constant current density of 10 mA cm^{-2} with 90% *iR*-compensation.

Note S3: Considering the coverage effect

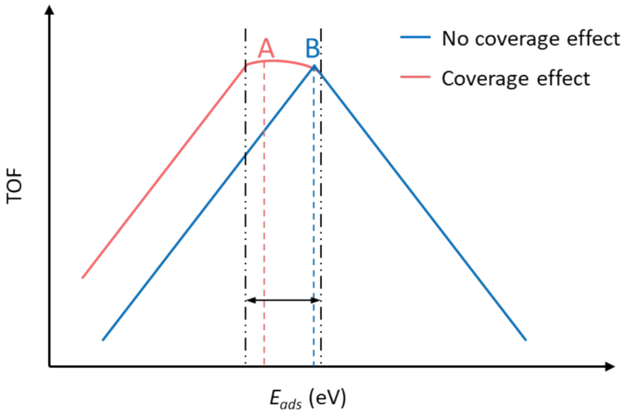

Fig. S1 Schematic diagram of volcanic curve considering the coverage effect or not. Point A and B indicate the best point of activity in each case.

Note S4: Elements of research

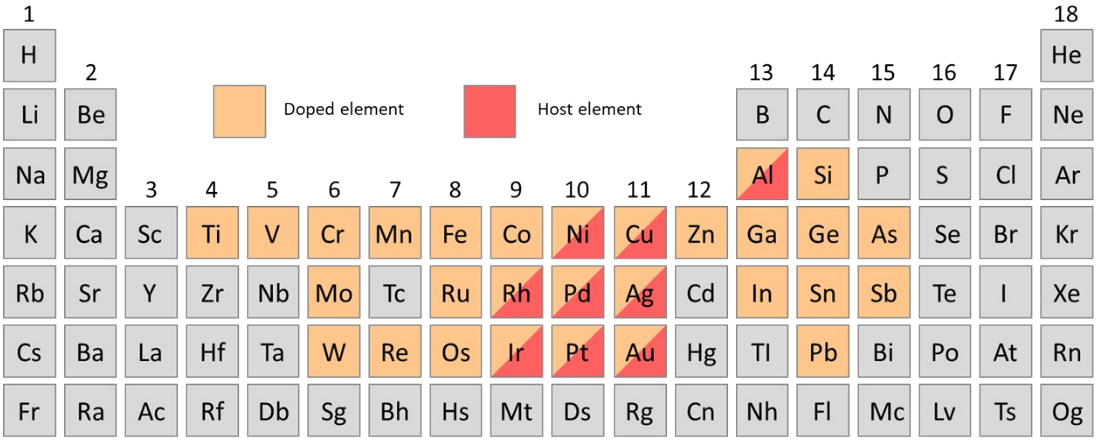

Fig. S2 Elements considered in this screening. Shading of element represents its inclusion in this screening study.

Note S5: A simple discussion the efficiency of the proposed optimization strategy compared to the pure exhaustive DFT calculations

In this work we try to figure out an important catalytic issue: What kind of single-atom alloys are more suitable for HER? The difficulty is, however, that the sample search space is too large to be explored exhaustively and the expert knowledge of structure-composition-activity remains far from sufficient. For example, with respect to the situation of ternary SAAs (a local site consists of one host metal and two guest metals), the search space could form ~8000 possibilities with a combination of 9 host-metals and 29/29 different guest metals (9*29*29=7569), leading to a great obstacle in screening promising catalyst with resorting to DFT calculations (see Fig. S3).

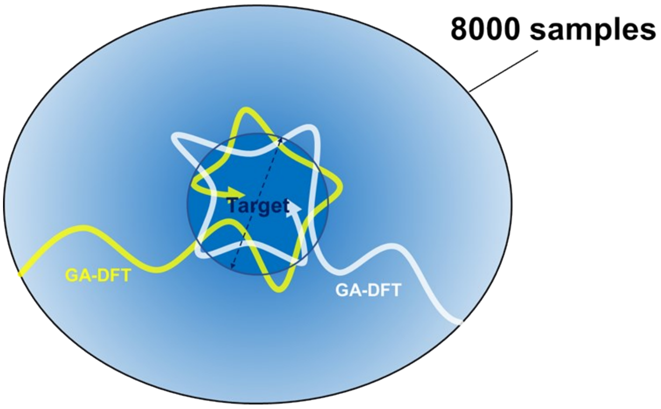

Fig. S3 A schematic diagram of genetic algorithm aided DFT calculations for searching the potential catalysts.

For the binary-SAA case, we performed one round of GA evolution for searching the target combinations, which consists of 20 generations with a population size of 10 configurations for each generation (total 200 sampling), and finally obtained 112 distinct binary SAAs. Thereinto, 70 candidate SAA catalysts were identified from these 112 DFT calculations (62.5% search success rate), as shown in Fig. S4a. However, the pure exhaustive DFT calculations including total 261 sampling (9*29) must be performed to determine the candidate binary SAA catalysts, leading to an extremely low screening efficiency. Moreover, the greater obstacle appears in the location of ternary SAAs, in which total 7569 sampling (9*29*29) should be verified by the exhaustive DFT calculations (see Fig. S4b). With our method, there are 1447 distinct ternary SAAs after 10 rounds of GA-DFT (total 2000 sampling), and 752 near-optimal surfaces out of these 1447 SAA catalysts were identified (52% search success rate). Overall, for a huge sample space, the proposed optimization strategy can search for catalysts more efficiently in comparison with the pure exhaustive method.

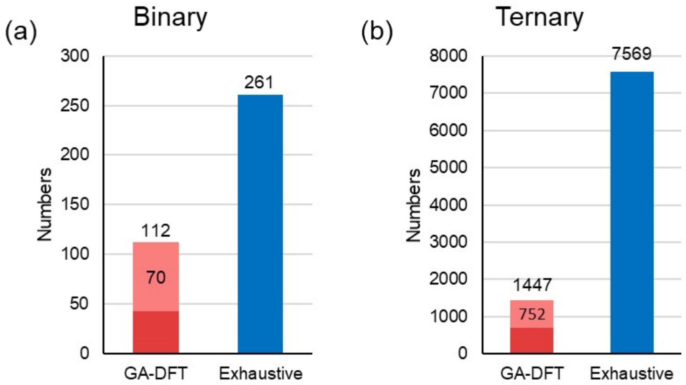

Fig. S4 A comparison between GA-DFT and exhaustive method for (a) binary and (b) ternary SAA catalysts.

Note S6: Calculating mixing energies

The mixing energies explain the thermodynamic requirements for the formation of SAA, in which a guest atom exchanges with a host atom, as shown in Fig. S5.

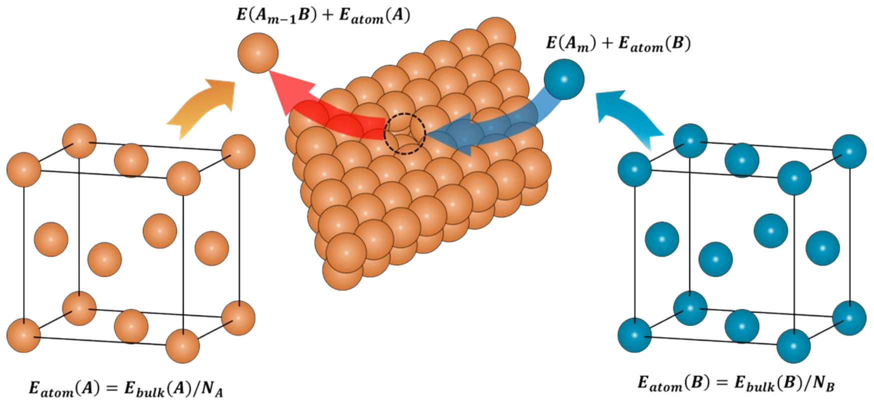

Fig. S5 Schematic diagram of the mixing energy calculation. $E(A_{m-1}B)$ and $E(A_m)$ are the total energies of surface of binary SAA and pure metal A, while $E_{atom}(A)$ and $E_{atom}(B)$ are the average energies of atom A and B relative to their bulk phase, respectively. The mixing energies reflect thermodynamic requirements for the formation of SAAs.

Note S7: Potential binary SAAs

Note that we have chosen surfaces whose energies are inside the range of -0.57 eV to -0.17 eV, the over-binding surfaces are more likely to perform well than under-binding surfaces due to the coverage effect. Our workflow identified 70 possible active surfaces, as shown in Table S1.

Table S1. List of 70 possible active surfaces for HER. All of the surfaces whose H adsorption energies are inside the range of (-0.57, -0.17) eV. H-G$_1$ represents the host metal with single guest atom. Note that, 46 highlighted rows indicate E_{mix} are less than zero, thereinto, 6 potential binary SAA catalysts are marked with dark green based on their cost-effective host metals (Ni and Cu).

H-G$_1$	E_H (eV)	E_{mix} (eV)	H-G$_1$	E_H (eV)	E_{mix} (eV)
Pt-Ti	-0.512	-2.887	Ir-Cr	-0.518	-0.281
Pd-Sb	-0.558	-2.652	Pd-Mo	-0.508	-0.267
Pd-Ga	-0.380	-2.308	Ni-Fe	-0.475	-0.237
Pt-Al	-0.417	-2.306	Ir-As	-0.253	-0.194

H-G$_1$	E$_H$ (eV)	E$_{mix}$ (eV)	H-G$_1$	E$_H$ (eV)	E$_{mix}$ (eV)
Pd-Ge	-0.341	-2.126	Pt-Au	-0.383	-0.169
Ir-Ti	-0.556	-2.087	Ir-Fe	-0.505	-0.108
Pd-Pb	-0.557	-2.078	Rh-Re	-0.499	-0.087
Ni-Al	-0.427	-1.657	Ir-Pd	-0.503	-0.087
Pt-Ga	-0.393	-1.628	Ir-Rh	-0.463	-0.080
Ir-Al	-0.345	-1.628	Pt-Cu	-0.509	-0.073
Rh-In	-0.545	-1.622	Ir-Au	-0.386	-0.046
Ni-Ga	-0.312	-1.521	Cu-Cu	-0.197	0.003
Pt-Pb	-0.281	-1.432	Ni-Ni	-0.541	0.004
Pt-V	-0.487	-1.327	Pt-Pt	-0.451	0.006
Ir-Ga	-0.302	-1.173	Ir-Cu	-0.495	0.093
Ir-In	-0.245	-1.153	Ir-Ni	-0.524	0.096
Pt-Zn	-0.448	-1.131	Ir-Co	-0.529	0.170
Ir-V	-0.543	-1.130	Ir-Ag	-0.457	0.239
Ni-In	-0.545	-1.123	Pt-Ni	-0.535	0.306
Pt-Ge	-0.387	-1.120	Al-W	-0.201	0.327
Ir-Si	-0.344	-0.932	Ag-Pt	-0.402	0.391
Ir-Ge	-0.267	-0.739	Pt-Re	-0.372	0.416
Pt-As	-0.454	-0.708	Ni-W	-0.567	0.430
Ir-Zn	-0.339	-0.689	Ni-Mo	-0.570	0.434
Pt-W	-0.391	-0.657	Cu-Ni	-0.507	0.455
Ni-Pt	-0.398	-0.642	Au-Pt	-0.402	0.690
Ir-Mo	-0.470	-0.617	Au-Ni	-0.268	1.034
Ir-W	-0.422	-0.587	Cu-Fe	-0.425	1.139
Rh-W	-0.556	-0.585	Pd-Os	-0.553	1.360
Ir-Mn	-0.516	-0.487	Au-Rh	-0.429	1.367
Rh-Pt	-0.487	-0.469	Au-Ru	-0.278	2.398
Pd-W	-0.456	-0.438	Ag-Ru	-0.502	2.856
Cu-Pt	-0.394	-0.400	Au-W	-0.259	3.266
Pd-Ag	-0.495	-0.325	Au-Re	-0.347	3.478
Ir-Pt	-0.392	-0.316	Ag-W	-0.502	4.473

Note S8: The catalytic performance of NiMo compared to the Pt

We evaluated the loading amount of NiMo catalyst via weighing 6 pieces of NiMo electrodes before and after fabrication, which indicates the final loading amount is ~6 mg cm^{-2}. For comparison, commercial Pt/C powder (5 wt%, Alfa Aesar) were dropped onto the Ni foam substrate with the same loading amount of 6 mg cm^{-2}. As shown in Fig. S6, the NiMo catalyst exhibits lower current density than the Pt/C control in the low overpotential range; however, when the potential increases, the NiMo catalyst delivers higher current density than the Pt/C control, which is consistent with the previous work[6].

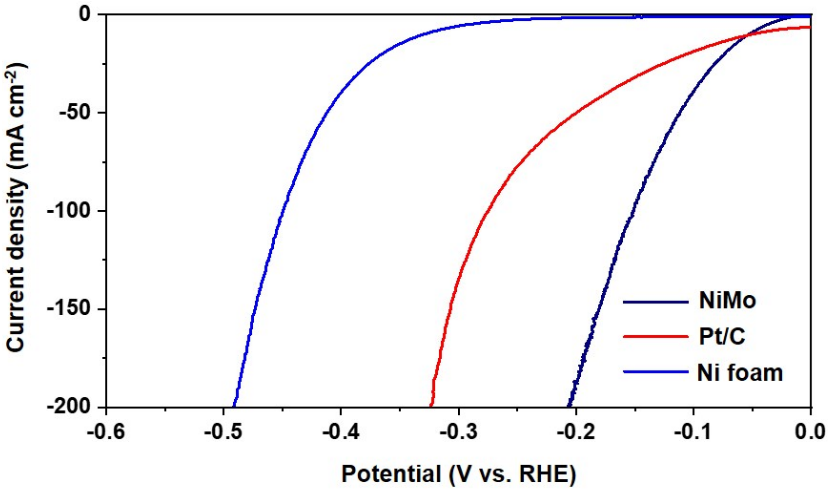

Fig. S6 LSV curves of NiMo, Pt/C and blank Ni foam, respectively. The loading amount of NiMo and Pt/C is ~6 mg cm^{-2}. All the data were obtained with the scan rate of 2 mV s^{-1}.

Note S9: A comparison between Ni-based bimetallic alloy and Ni-based single atom alloy

To demonstrate the Ni/Mo atomic distribution, we conducted additional HAADF-STEM image of NiMo alloy (Fig. S7), which also suggests the overlaps of Mo and Ni elements over the sample.

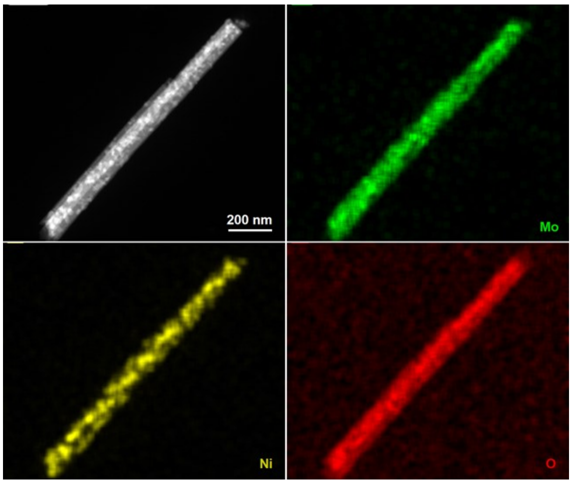

Fig. S7 Typical HAADF-STEM image of NiMo alloy sample and corresponding elemental maps of Mo, Ni, and O, respectively.

Nevertheless, we acknowledge that we haven't provided direct evidence for characterization of single atom alloy (SAA); we in fact fabricated Ni-based bimetallic alloy, instead of Ni-based single atom alloy, and demonstrated the homogeneous distribution of the guest elements. Specifically, in the previous version, we systematically characterized the NiMo-based bimetallic alloys, and illustrated that the catalyst, serving as the homogeneously dispersed alloy which contains SAA motif, would be a superior HER catalyst. To further verify this concept, we now synthesized NiAl-based bimetallic alloy with different molar ratios. In Fig. S8, the Ni_3Al electrocatalyst exhibits higher activities in both low and high overpotential regions than those of other NiAl samples with higher Al content (e.g., NiAl, $NiAl_3$ and $NiAl_5$), which indicates that maximizing the dispersion of Al atom in the bimetallic alloy can obtain more active sites for better HER performance. In Figs. S9-S11, we collected HAADF-STEM images of Ni_3Al sample at different magnification, and demonstrated the homogenous dispersion of Ni and Al elements in the EDS maps. In addition, the molar ratio of Ni:Al of Ni_3Al sample was determined to be 3:1 in the EDS result (Fig. S12); as the atomic configuration of Ni_3Al-alloy shows in Fig. S13, it corresponds to the existence of active Ni_2Al_1 fcc-site, which is the basic motif of NiAl SAA.

Moreover, we performed the theoretical studies to compare the activities between highly dispersed NiAl-alloys and single atom NiAl-alloys (see Fig. S13). First, we considered the H adsorption energy (E_H) on the fcc-hollow site of Ni(111) with only one-, two- or three-Al doped, forming the Ni_2Al_1, Ni_1Al_2 and Al_3 local site, respectively, as shown in Fig. S13a-S13c. It reveals that the introduction of more Al atoms into the fcc-hollow site would significantly weaken the H adsorption. Notably, E_H on the Al_1Ni_2 site is -0.43 eV (see Fig. S13a), which is inside the range of the target search space [-0.57, -0.17] eV. In contrast, the Ni_1Al_2 and Al_3 site results in excessively weak E_H and precludes their high activity for HER (-0.14/0.10 eV, respectively; see Figs. S13b and S13c). Therefore, a higher HER performance could be expected by constructing NiAl SAA catalyst. Second, we also investigated the E_H on other atomically dispersed NiAl alloys, i.e., 25%, 50% and 75% Al are doped into the Ni bulk (see Fig. S13d-S13g), corresponding to Ni_3Al-, NiAl- and $NiAl_3$-alloy, respectively. In the same vein, the E_H becomes more positive as the number of doped Al atoms increases, ranking in the order of 25% Al (-0.41 eV) < 50% Al (-0.40 eV, 0.00 eV) < 75% Al (0.37 eV). Remarkably, on the local Ni_2Al_1 site of either SAA or NiAl-alloys (Ni_3Al, NiAl), the E_H are basically the same (see Fig. S13a, S13d, S13e) and within the active region of [-0.57, -0.17] eV, indicating that the local Ni_2Al_1 site largely determines the H adsorption strength, although there are excess Al atoms in the bulk phase for the Ni_3Al- and NiAl-alloys. Thus, these results reveal that, for the NiAl alloys or SAA, **the single-Al-atom fcc site (Ni_2-Al_1) is the key to realize the high-performance for HER.** Overall, these theoretical insights are consistent with the experiment results above; the HER activity can be improved by suitably reducing the Al load, which essentially increases the dispersion of Al on the surfaces (and thus the number of Ni_2Al_1 site), and thus confirms the rationality of our method for material screening. Our ongoing work is to further control the atom dispersion and construct real single atom alloy catalyst, to extremely boost electrocatalytic hydrogen evolution reaction.

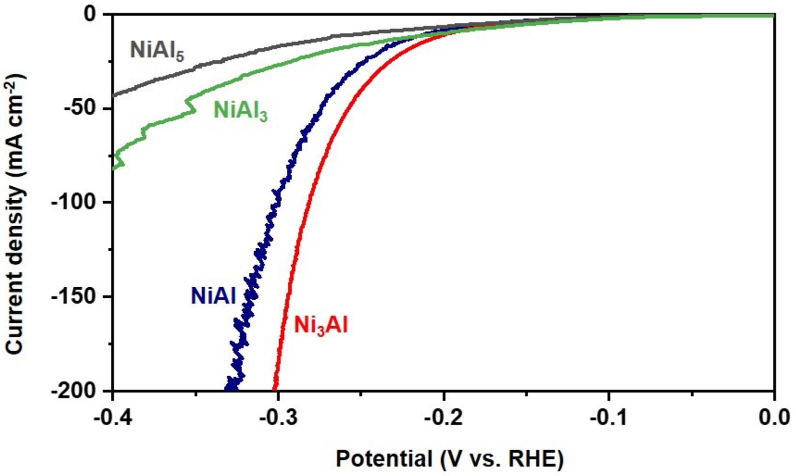

Fig. S8 LSV curves of Ni_3Al bimetallic alloy samples and NiAl, $NiAl_3$ and $NiAl_5$ controls, respectively.

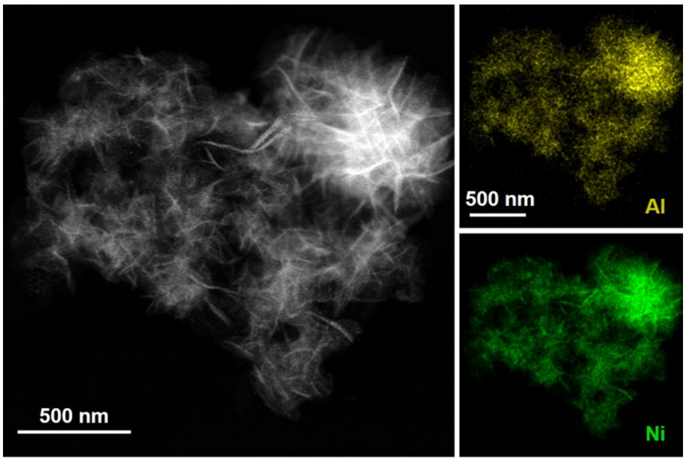

Fig. S9 HAADF-STEM image of Ni_3Al sample and corresponding elemental maps of Al and Ni.

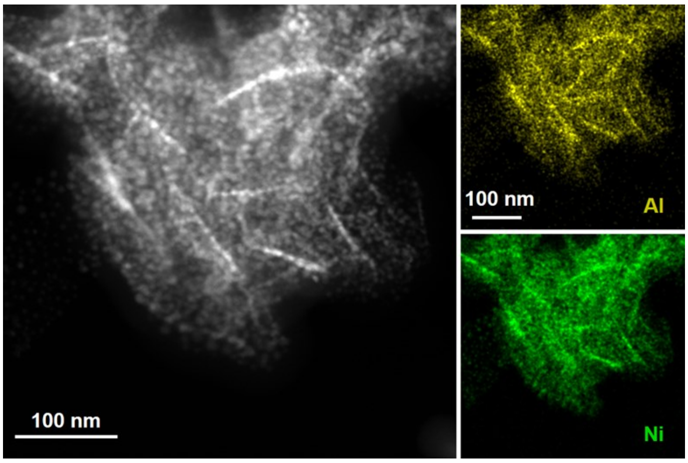

Fig. S10 HAADF-STEM image of Ni_3Al sample and corresponding elemental maps of Al and Ni.

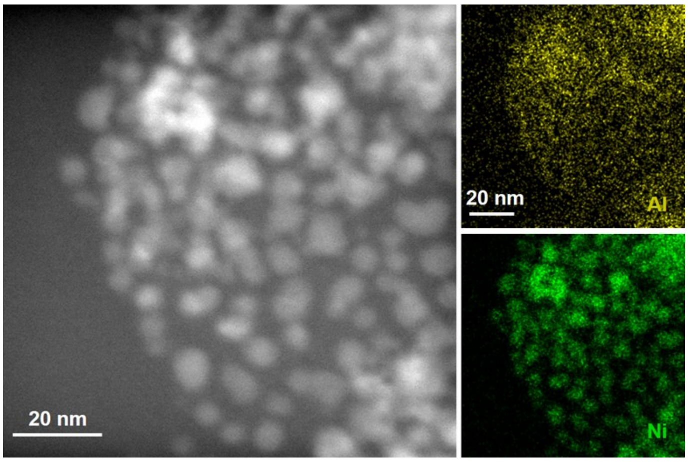

Fig. S11 HAADF-STEM image of Ni_3Al sample and corresponding elemental maps of Al and Ni.

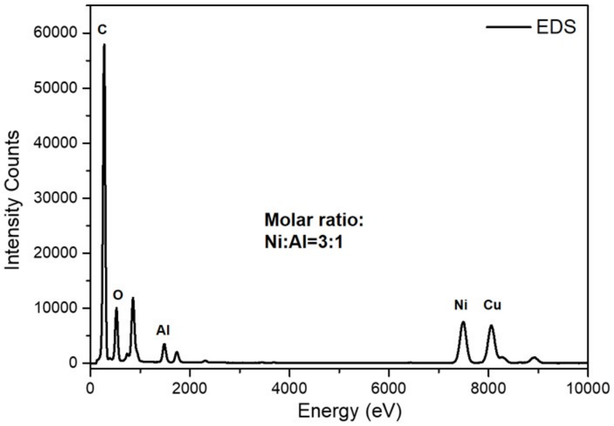

Fig. S12 EDS spectra of Ni_3Al catalyst, which indicates the molar ratio of Ni:Al is 3:1 in the sample.

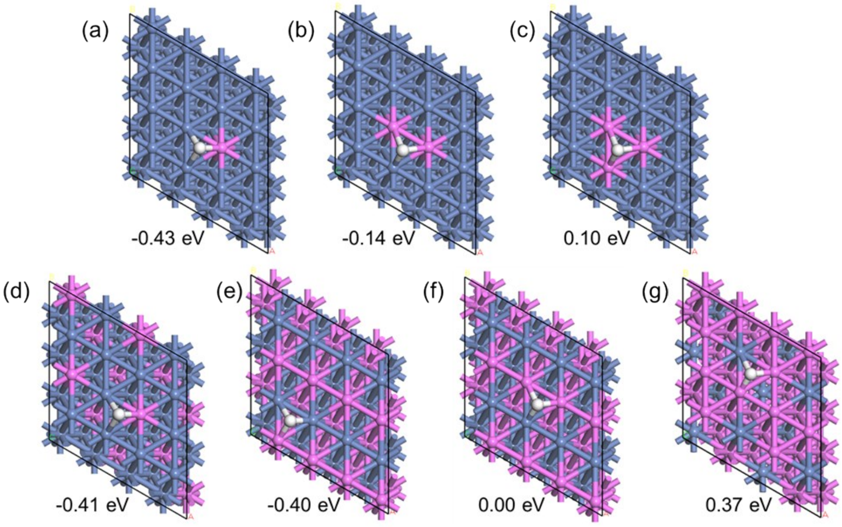

Fig. S13 Hydrogen adsorption structures of different atomically dispersed NiAl alloys with the H adsorption energy (E_H) given. (a-c) correspond to one-, two- and three-Al doped into the surface of Ni(111), respectively, while (d-g) are the NiAl-alloys with (d) 25% Al, (e, f) 5% Al, (g) 75% Al, respectively. White, blue and pink balls indicate H, Ni and Al, respectively.

Note S10: HER performance evaluation of Ni-based category

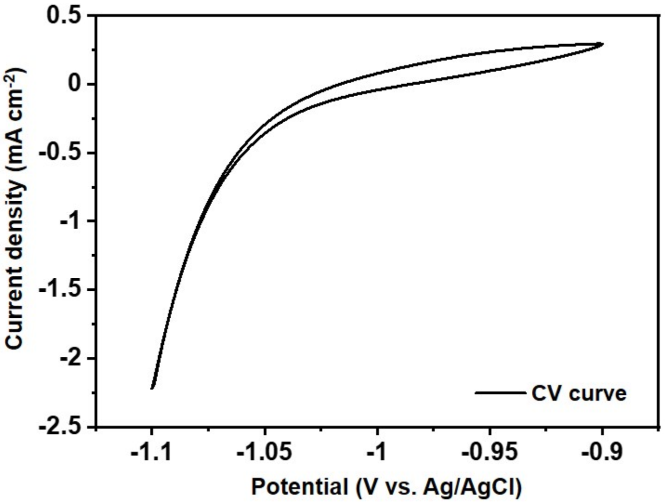

Fig. S14 The calibration of Ag/AgCl/3.5 M KCl reference electrode with respect to RHE. In the 1.0 M KOH, $E_{RHE} = E_{Ag/AgCl} + 1.001$ V.

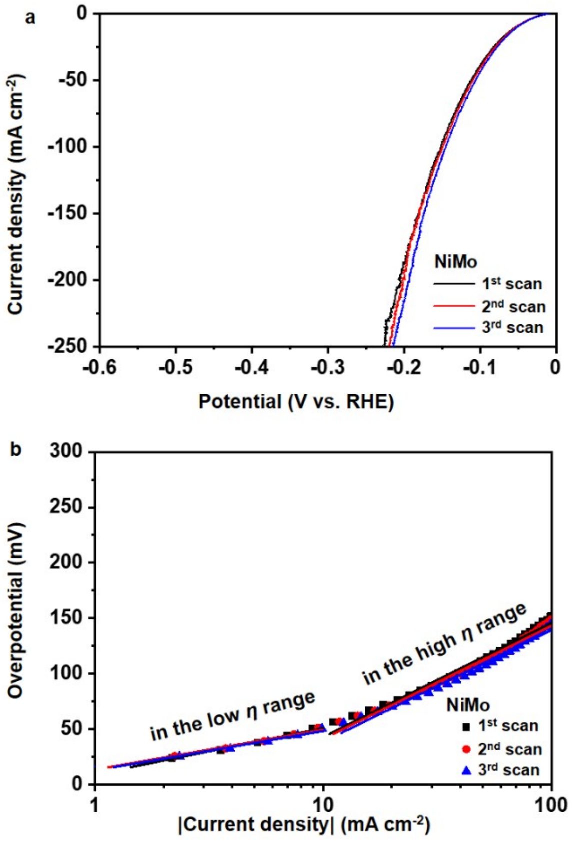

Fig. S15 (a) The LSV curves of NiMo bimetallic electrocatalyst and (b) corresponding derived Tafel slope plots, which were collected for three independent tests.

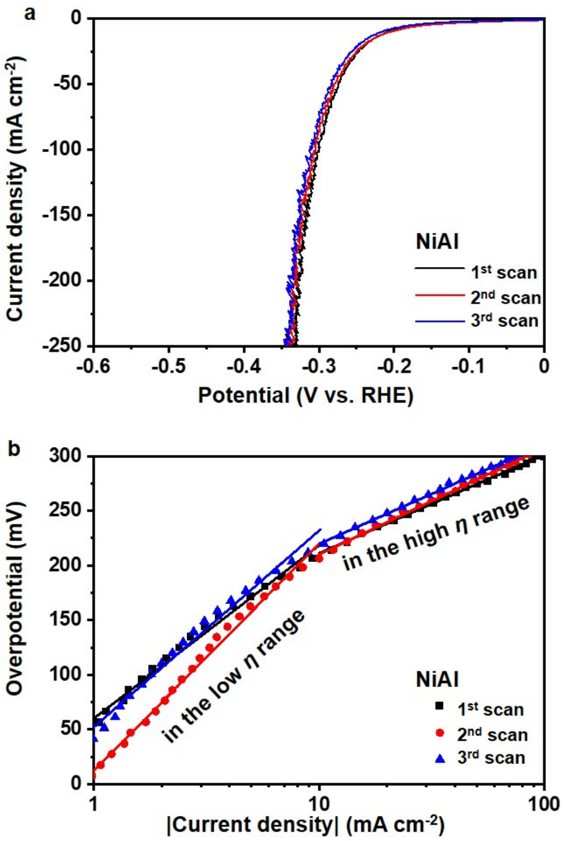

Fig. S16 (a) The LSV curves of NiAl bimetallic electrocatalyst and (b) corresponding derived Tafel slope plots, which were collected for three independent tests.

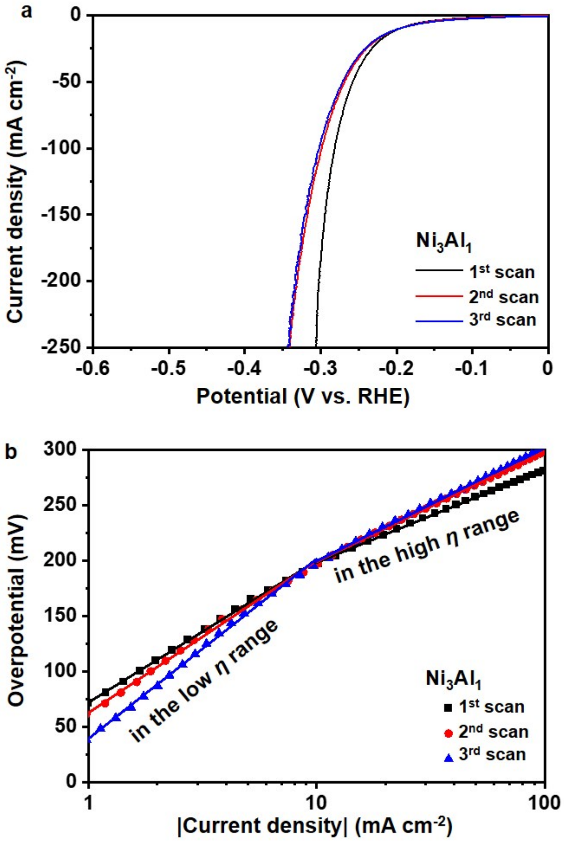

Fig. S17 (a) The LSV curves of Ni_3Al bimetallic electrocatalyst and (b) corresponding derived Tafel slope plots, which were collected for three independent tests.

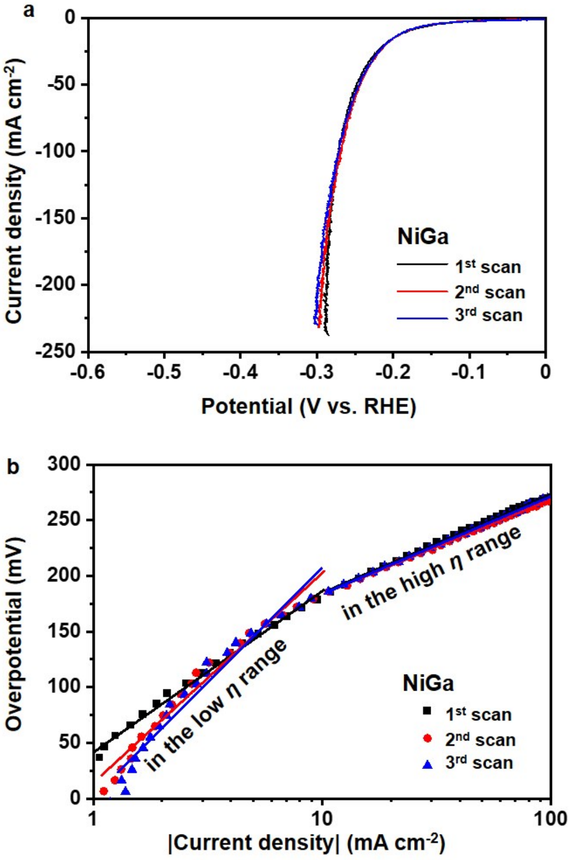

Fig. S18 (a) The LSV curves of NiGa bimetallic electrocatalyst and (b) corresponding derived Tafel slope plots, which were collected for three independent tests.

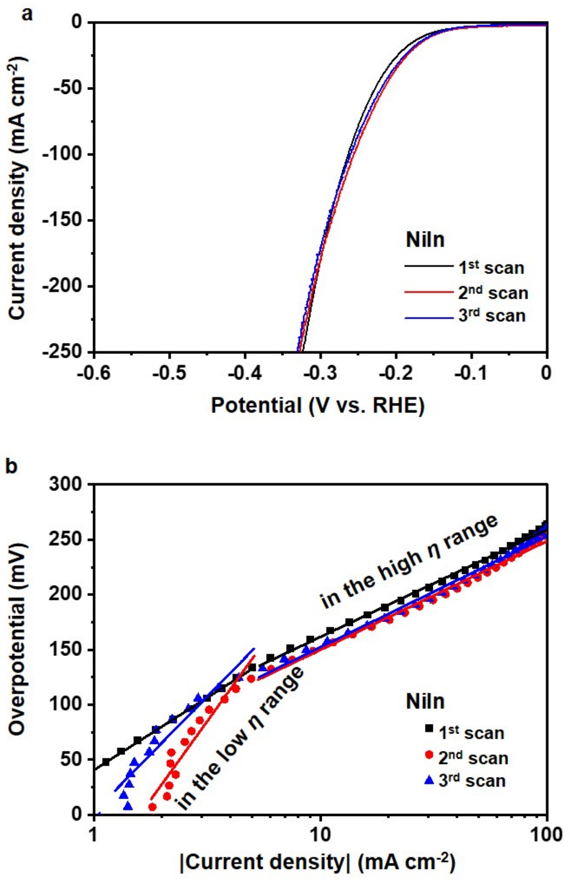

Fig. S19 (a) The LSV curves of NiIn bimetallic electrocatalyst and (b) corresponding derived Tafel slope plots, which were collected for three independent tests.

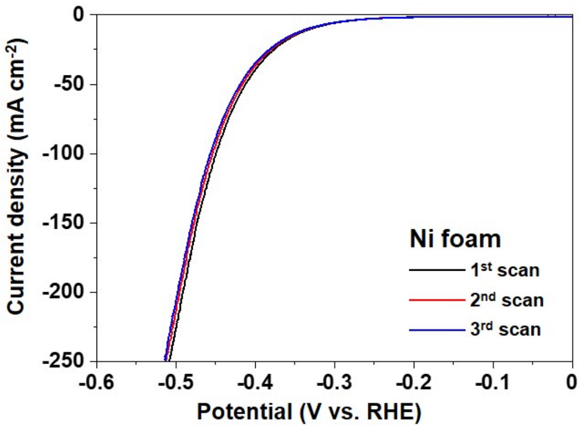

Fig. S20 The LSV curves of bare Ni foam collected for three independent tests.

Table S2. The summarized HER performances of synthesized Ni-based bimetallic electrocatalysts, showing the Tafel slopes in the different overpotential regions and the overpotentials to achieve 10, 50, 100 and 200 mA cm^{-2}.

Electrocatalysts	η_{10} **(mV)**	η_{50} **(mV)**	η_{100} **(mV)**	η_{200} **(mV)**	**Tafel slope$_1$ （mV dec^{-1}）**	**Tafel slope$_2$ （mV dec^{-1}）**
bare Ni foam	-332.23 ± 2.05	-416.19 ± 3.46	-453.31 ± 3.55	-495.03 ± 3.25	/	/
Ni$_3$Al	-197.22 ± 0.58	-265.69 ± 7.17	-293.98 ± 11.04	-321.72 ± 16.82	142.26 ± 17.78	95.25 ± 9.72
NiAl	-210.69 ± 5.80	-279.52 ± 4.84	-304.83 ± 5.72	-330.61 ± 6.01	181.89 ± 24.91	93.18 ± 4.10
NiGa	-182.76 ± 1.33	-245.15 ± 2.62	-270.26 ± 1.47	-292.59 ± 4.18	179.60 ± 31.32	87.23 ± 1.93
NiIn	-156.78 ± 5.75	-221.26 ± 6.08	-260.12 ± 3.90	-309.87 ± 2.78	208.94 ± 77.10	98.89 ± 1.74
NiMo	-52.32 ± 1.12	-109.14 ± 3.22	-148.54 ± 2.99	-200.06 ± 6.69	37.84 ± 3.39	102.05 ± 1.16

Notes: η_{10}, $\eta_{50,}$ η_{100} and η_{200} mean the overpotentials to achieve the current densities of 10, 50, 100 and 200 mA cm^{-2}, respectively; Tafel slope$_1$ and Tafel slope$_2$ mean the values calculated in the low and high potential regions, respectively.

Note S11: Potential ternary SAAs

Likewise, our workflow identified 752 possible active surfaces, as shown in Table S3.

Table S3. List of 752 possible active surfaces for HER. All of the surfaces whose H adsorption energies are inside the range of (-0.57, -0.17) eV. H-G$_1$-G$_2$ represents the host metal with two guest atoms. Note that, 504 highlighted rows indicate E_{mix} are less than zero, thereinto, 142 potential binary SAA catalysts are marked with dark green based on their cost-effective host metals (Al, Ni and Cu).

H-G$_1$-G$_2$	**E$_H$ (eV)**	**E$_{mix}$ (eV)**	**H-G$_1$-G$_2$**	**E$_H$ (eV)**	**E$_{mix}$ (eV)**
Pt_Ti_Pb	-0.367	-4.171	Pd_Fe_Pd	-0.502	-0.458
Pd_Zn_Ti	-0.171	-3.968	Rh_Ag_W	-0.438	-0.456
Pd_Ti_Zn	-0.172	-3.967	Ir_As_Re	-0.304	-0.455
Rh_Si_Al	-0.265	-3.890	Ir_Mo_Re	-0.518	-0.450
Pt_Si_Al	-0.503	-3.770	Ni_Ni_Au	-0.262	-0.440
Rh_Ge_Al	-0.244	-3.720	Pd_W_Pd	-0.456	-0.438
Rh_In_Al	-0.269	-3.573	Ir_Re_Mn	-0.525	-0.436
Rh_Ti_Pb	-0.292	-3.558	Ni_Cu_Pd	-0.314	-0.433
Pt_Ge_Al	-0.443	-3.526	Pd_Cu_Mo	-0.384	-0.429
Pt_Al_Zn	-0.504	-3.400	Ni_W_Pb	-0.495	-0.423
Pt_Zn_Al	-0.505	-3.400	Ir_Pt_Rh	-0.475	-0.420
Ir_Si_Ti	-0.503	-3.321	Pt_Cu_Fe	-0.440	-0.406
Pt_Ga_Si	-0.492	-3.166	Pd_Co_Au	-0.274	-0.406
Rh_V_Al	-0.407	-3.143	Ni_Au_Co	-0.208	-0.402
Pt_Al_Mn	-0.524	-3.141	Ni_Co_Au	-0.209	-0.401
Pt_Mn_Al	-0.523	-3.141	Rh_Au_Rh	-0.367	-0.401
Rh_Zn_Ti	-0.412	-3.138	Ir_W_Re	-0.488	-0.400
Rh_Ti_Zn	-0.412	-3.138	Cu_Cu_Pt	-0.394	-0.400
Pd_Au_Ti	-0.272	-3.134	Ni_Cr_Zn	-0.428	-0.399
Rh_Zn_Al	-0.254	-3.003	Ir_W_Cu	-0.506	-0.390
Pd_Sn_Ag	-0.479	-2.924	Al_W_Au	-0.323	-0.389
Pt_Ti_W	-0.409	-2.923	Rh_Pt_Ir	-0.425	-0.388
Pt_Ti_Pd	-0.531	-2.908	Al_Au_W	-0.327	-0.387
Pt_Cu_Ti	-0.479	-2.908	Al_Mo_Re	-0.262	-0.385
Pd_Ag_Ti	-0.303	-2.863	Al_Mo_Cu	-0.210	-0.385
Ir_Al_Si	-0.508	-2.839	Ir_Zn_Ag	-0.429	-0.385
Rh_Zn_Si	-0.239	-2.825	Rh_Au_Re	-0.310	-0.380
Pd_Cu_Sb	-0.503	-2.806	Rh_Re_Au	-0.310	-0.379
Pd_Cu_Ti	-0.433	-2.764	Ir_Cr_Pd	-0.550	-0.377

H-G$_1$-G$_2$	**E$_H$ (eV)**	**E$_{mix}$ (eV)**	**H-G$_1$-G$_2$**	**E$_H$ (eV)**	**E$_{mix}$ (eV)**
Rh_Zn_Ga	-0.270	-2.723	Pt_Au_Ag	-0.313	-0.374
Ni_Al_Ti	-0.398	-2.717	Rh_Mo_Re	-0.549	-0.373
Pd_Al_Pd	-0.413	-2.672	Ir_Au_As	-0.203	-0.367
Pd_Sb_Pd	-0.558	-2.652	Ir_As_Ni	-0.433	-0.363
Al_Ti_Pt	-0.200	-2.644	Rh_Au_Ag	-0.210	-0.362
Pt_Cr_Al	-0.507	-2.642	Pd_Pt_Ag	-0.556	-0.357
Pt_Mo_Al	-0.325	-2.629	Pd_Ag_Pt	-0.555	-0.357
Rh_Zn_As	-0.209	-2.604	Pd_Cr_Ag	-0.376	-0.357
Pd_Cr_Sn	-0.172	-2.597	Ir_Au_Cr	-0.392	-0.344
Rh_Au_Ti	-0.363	-2.597	Ir_Cr_Au	-0.393	-0.344
Pd_Pt_Sb	-0.563	-2.584	Cu_Ti_Pt	-0.254	-0.343
Pd_Sb_Pt	-0.562	-2.584	Pt_Ga_Os	-0.285	-0.334
Rh_Al_Mn	-0.380	-2.553	Rh_Au_Ni	-0.363	-0.329
Ir_Pt_Ti	-0.499	-2.514	Pd_Pd_Ag	-0.496	-0.325
Rh_Pt_Al	-0.469	-2.511	Rh_Cr_Cu	-0.519	-0.321
Rh_Mo_Al	-0.386	-2.499	Rh_Mn_Co	-0.442	-0.318
Pd_Cu_In	-0.525	-2.494	Ir_Pt_Ir	-0.392	-0.316
Pd_Cu_Ga	-0.219	-2.474	Rh_Ni_Au	-0.376	-0.314
Pd_Zn_V	-0.172	-2.472	Pd_Ni_Au	-0.368	-0.309
Pt_Ag_Al	-0.474	-2.471	Cu_Ag_Pt	-0.336	-0.305
Ni_Pb_Al	-0.377	-2.455	Pd_Cr_W	-0.427	-0.303
Rh_Au_Al	-0.206	-2.440	Rh_Au_Ir	-0.436	-0.298
Rh_Sn_W	-0.293	-2.431	Pt_Mn_Re	-0.408	-0.298
Rh_W_Si	-0.344	-2.393	Ni_Pd_Ni	-0.435	-0.296
Pt_Al_Pd	-0.415	-2.387	Ni_Ni_Pd	-0.436	-0.295
Rh_Si_Mo	-0.336	-2.376	Ni_Mn_Co	-0.487	-0.286
Ir_Si_Ga	-0.489	-2.365	Ni_Co_Mn	-0.481	-0.286
Ni_Pt_Al	-0.328	-2.361	Ir_W_Co	-0.562	-0.285
Pd_Pd_In	-0.399	-2.341	Ir_Cr_Ir	-0.518	-0.281
Pt_V_Zn	-0.511	-2.338	Ni_Pd_Co	-0.373	-0.280
Ir_Zn_Al	-0.261	-2.336	Al_Zn_Mo	-0.180	-0.268
Pd_Ti_Mo	-0.440	-2.336	Ir_Pt_Ni	-0.494	-0.268
Pd_Ga_Pd	-0.380	-2.308	Ir_Mo_Ag	-0.497	-0.255
Pt_Al_Pt	-0.417	-2.306	Pt_Mo_Rh	-0.492	-0.255
Pd_Cr_Ga	-0.189	-2.292	Ni_Zn_Mo	-0.425	-0.253
Pd_Co_Ti	-0.416	-2.276	Ni_Mo_Zn	-0.425	-0.253
Rh_Al_Pd	-0.382	-2.274	Rh_Ag_Cr	-0.432	-0.252
Rh_W_Ga	-0.379	-2.252	Pt_Mo_Ni	-0.498	-0.247
Pd_Cr_In	-0.225	-2.235	Pt_Au_Pd	-0.389	-0.240
Rh_Ti_Cu	-0.566	-2.218	Pt_Pd_Au	-0.389	-0.240
Rh_Ge_Mo	-0.333	-2.198	Cu_Cu_Pd	-0.334	-0.230
Pd_Si_Pd	-0.337	-2.192	Ir_Fe_Pd	-0.508	-0.226
Ir_Au_Ti	-0.410	-2.185	Cu_Ni_Zn	-0.294	-0.222

H-G$_1$-G$_2$	E_H (eV)	E_{mix} (eV)	H-G$_1$-G$_2$	E_H (eV)	E_{mix} (eV)
Ir_Al_W	-0.426	-2.178	Cu_Mn_Sn	-0.176	-0.217
Ir_W_Al	-0.428	-2.178	Pt_Re_As	-0.423	-0.216
Pd_Pt_Si	-0.498	-2.173	Ir_Pt_Co	-0.453	-0.211
Ni_Pt_Ge	-0.405	-2.163	Cu_Ge_Ir	-0.565	-0.196
Ni_Au_Si	-0.340	-2.162	Cu_Pb_Rh	-0.461	-0.196
Al_Mo_Rh	-0.182	-2.152	Rh_Pd_Ag	-0.410	-0.194
Rh_Si_Au	-0.246	-2.151	Ir_Au_Pd	-0.346	-0.173
Ni_Ga_Pt	-0.290	-2.141	Ir_Pd_Au	-0.344	-0.173
Rh_V_Zn	-0.408	-2.127	Al_Mo_Mn	-0.345	-0.171
Pd_Ge_Pd	-0.341	-2.126	Ir_Ru_As	-0.303	-0.169
Pd_Al_Rh	-0.446	-2.097	Al_V_Re	-0.379	-0.168
Rh_Cr_Si	-0.343	-2.096	Al_Re_V	-0.377	-0.166
Pd_Pb_Pd	-0.557	-2.078	Ni_Ag_Pd	-0.267	-0.155
Rh_Mo_As	-0.540	-2.077	Ir_Rh_Au	-0.418	-0.154
Pt_Au_Sn	-0.405	-2.058	Ir_Ru_Pt	-0.431	-0.153
Rh_In_Mo	-0.341	-2.058	Ir_Pt_Ru	-0.431	-0.153
Rh_In_Pt	-0.478	-2.043	Rh_W_Ru	-0.560	-0.153
Rh_Ag_Al	-0.242	-2.041	Ni_Fe_Co	-0.451	-0.149
Ni_V_As	-0.560	-2.039	Pd_Cr_Mo	-0.478	-0.146
Pd_Zn_Au	-0.180	-2.029	Ir_Os_Mo	-0.525	-0.141
Pd_Au_Zn	-0.181	-2.029	Ir_Re_Ir	-0.402	-0.136
Rh_Rh_Al	-0.440	-2.028	Pt_Cu_Pd	-0.525	-0.133
Pt_Cr_Ga	-0.492	-2.028	Pd_Cr_Cr	-0.463	-0.130
Pd_Pb_Pt	-0.560	-2.026	Ir_Cu_Cr	-0.538	-0.129
Ni_Al_Pd	-0.275	-2.023	Ir_Pt_Ag	-0.361	-0.127
Ni_Pd_Al	-0.275	-2.023	Ni_Ni_Cu	-0.430	-0.124
Ni_As_Mn	-0.514	-2.020	Rh_Pt_Ru	-0.455	-0.118
Pt_Re_Ti	-0.459	-2.015	Ir_W_Os	-0.478	-0.109
Rh_Cr_Ga	-0.372	-2.000	Ir_Ir_Fe	-0.505	-0.108
Rh_Au_Ge	-0.213	-1.994	Ir_Re_Au	-0.370	-0.106
Al_Mo_Ir	-0.172	-1.988	Pd_Ni_Ag	-0.437	-0.100
Rh_Zn_Zn	-0.194	-1.983	Pt_Os_Pb	-0.288	-0.099
Ni_Zn_Ti	-0.370	-1.977	Pd_W_Ni	-0.471	-0.091
Ir_Sn_Mo	-0.330	-1.962	Pd_W_W	-0.463	-0.078
Ir_Mo_Sn	-0.334	-1.961	Au_Ti_Ti	-0.497	-0.070
Pt_Au_In	-0.249	-1.959	Ir_Re_Fe	-0.523	-0.065
Rh_In_Au	-0.174	-1.950	Ir_Fe_Re	-0.524	-0.065
Rh_Ge_Cr	-0.341	-1.946	Cu_Au_Ni	-0.297	-0.055
Rh_Al_Ir	-0.546	-1.945	Rh_Re_Ir	-0.435	-0.047
Ni_Al_Mn	-0.325	-1.927	Ir_Au_Ir	-0.386	-0.046
Ni_Sb_Pd	-0.401	-1.926	Pd_Au_Rh	-0.402	-0.040
Ni_Pd_Sb	-0.403	-1.925	Pd_W_Mo	-0.506	-0.040
Rh_Ni_Al	-0.469	-1.920	Pd_Rh_Au	-0.401	-0.039

H-G$_1$-G$_2$	E$_H$ (eV)	E$_{mix}$ (eV)	H-G$_1$-G$_2$	E$_H$ (eV)	E$_{mix}$ (eV)
Ir_Ti_Re	-0.566	-1.910	Al_Mn_Ga	-0.205	-0.034
Ir_Re_Ti	-0.567	-1.910	Pt_Pt_Pd	-0.518	-0.032
Ni_Ge_Pd	-0.452	-1.891	Ir_Au_Au	-0.181	-0.029
Ni_Pd_Ge	-0.454	-1.891	Rh_Au_Ru	-0.350	-0.028
Pt_In_Pd	-0.374	-1.887	Pt_Co_Fe	-0.462	-0.028
Rh_Si_Re	-0.351	-1.861	Al_Mn_Pb	-0.218	-0.024
Ni_Au_Ge	-0.328	-1.855	Ir_Cu_Pd	-0.466	-0.019
Al_Mo_Pd	-0.185	-1.853	Rh_Ag_Rh	-0.473	-0.016
Ni_Au_As	-0.315	-1.852	Rh_Co_Au	-0.395	-0.009
Rh_Au_As	-0.243	-1.846	Rh_Au_Co	-0.396	-0.009
Rh_In_Cr	-0.344	-1.846	Al_Mo_Cr	-0.422	-0.003
Rh_Si_Ag	-0.266	-1.845	Ir_Pt_Os	-0.364	-0.003
Pt_Ag_Ga	-0.463	-1.839	Ni_Cr_Au	-0.329	-0.001
Ir_Al_Pd	-0.347	-1.835	Cu_Ni_Pt	-0.512	0.008
Ni_Mn_Ga	-0.204	-1.832	Ir_Ni_Au	-0.372	0.012
Pt_Au_Ga	-0.293	-1.829	Rh_Re_Re	-0.475	0.018
Ni_Pd_Sn	-0.414	-1.818	Ir_Ni_Re	-0.549	0.020
Ni_V_Al	-0.419	-1.810	Ni_Pt_Ru	-0.396	0.025
Ir_Co_Ti	-0.566	-1.810	Rh_Ni_Re	-0.555	0.035
Ni_Au_Sb	-0.265	-1.808	Cu_Al_Ti	-0.343	0.045
Ni_Si_Ir	-0.421	-1.803	Cu_Mn_Pd	-0.246	0.060
Pd_Al_Re	-0.398	-1.802	Rh_Ir_Ag	-0.484	0.070
Rh_Si_Rh	-0.430	-1.793	Rh_Ag_Ir	-0.485	0.070
Pt_Si_Cr	-0.477	-1.782	Rh_Ag_Ni	-0.472	0.071
Ni_Fe_As	-0.487	-1.781	Cu_Pt_Rh	-0.396	0.071
Ni_Sn_V	-0.536	-1.777	Ir_Os_As	-0.272	0.073
Pt_Cu_Ga	-0.476	-1.773	Ir_Au_Cu	-0.297	0.077
Pt_Si_Mo	-0.440	-1.768	Pt_Ni_Au	-0.399	0.083
Ir_Al_Rh	-0.375	-1.758	Ni_Ag_Co	-0.309	0.093
Ir_Mo_In	-0.358	-1.757	Ni_Co_Ag	-0.310	0.093
Ni_Fe_Al	-0.293	-1.745	Ir_Co_Au	-0.372	0.106
Ni_Cu_As	-0.474	-1.742	Ir_Au_Co	-0.370	0.106
Ir_Al_Re	-0.379	-1.736	Cu_Co_Al	-0.444	0.106
Ni_Rh_Al	-0.385	-1.733	Cu_Cr_Sb	-0.245	0.110
Ir_Au_Al	-0.196	-1.725	Rh_Os_Au	-0.365	0.118
Ir_Al_Au	-0.191	-1.725	Ni_Au_Mo	-0.329	0.122
Ni_Pt_In	-0.386	-1.708	Ni_Mo_Au	-0.332	0.125
Rh_Ag_Ge	-0.250	-1.699	Ir_Ru_Re	-0.500	0.130
Pt_Al_Re	-0.273	-1.684	Rh_Ni_Ir	-0.557	0.133
Pt_Re_Al	-0.262	-1.684	Ni_W_Au	-0.316	0.137
Ir_W_In	-0.332	-1.681	Ni_Ru_V	-0.550	0.138
Pd_Zn_Cu	-0.300	-1.681	Ni_V_Ru	-0.550	0.138
Ni_As_Rh	-0.505	-1.677	Ni_Cr_Pd	-0.509	0.154

H-G_1-G_2	E_H (eV)	E_{mix} (eV)	H-G_1-G_2	E_H (eV)	E_{mix} (eV)
Ni_Ni_As	-0.543	-1.675	Ir_Ru_Au	-0.411	0.157
Ni_As_Ni	-0.541	-1.674	Ir_Au_Ru	-0.411	0.157
Rh_Pb_Au	-0.384	-1.663	Ir_Fe_Ru	-0.556	0.158
Rh_Al_Ru	-0.416	-1.642	Pd_Au_Re	-0.241	0.161
Rh_Ru_Al	-0.416	-1.641	Ni_Ag_Ir	-0.407	0.167
Ni_Ti_Pd	-0.434	-1.636	Ir_Ag_Fe	-0.434	0.182
Ni_Pd_Ti	-0.435	-1.635	Pd_Mo_Rh	-0.530	0.186
Ir_Si_Mn	-0.487	-1.630	Pt_Re_Cr	-0.444	0.188
Ir_W_Si	-0.419	-1.616	Ni_Mo_Pd	-0.486	0.212
Rh_Ru_Sn	-0.489	-1.608	Pt_Cu_Ni	-0.555	0.225
Rh_Ag_As	-0.237	-1.597	Ir_Ag_Re	-0.469	0.229
Pd_Zn_Mo	-0.187	-1.596	Cu_Pd_Ni	-0.544	0.235
Pd_V_Au	-0.258	-1.591	Ir_Ag_Ir	-0.457	0.239
Ni_Pb_Pt	-0.328	-1.587	Pt_Ag_Rh	-0.522	0.240
Rh_Au_V	-0.331	-1.577	Ir_Ni_Cu	-0.521	0.240
Rh_V_Au	-0.331	-1.576	Ir_Ag_Au	-0.254	0.262
Pd_Ru_Al	-0.345	-1.564	Ir_Au_Ag	-0.254	0.262
Ir_Ni_Al	-0.411	-1.563	Ir_Os_Re	-0.430	0.273
Ir_Al_Ni	-0.410	-1.563	Pd_Ir_W	-0.519	0.280
Ir_Cr_Ga	-0.406	-1.550	Rh_Ru_Re	-0.512	0.297
Pt_Cu_Si	-0.468	-1.545	Pd_Ir_Au	-0.527	0.301
Ir_Cu_Al	-0.381	-1.540	Al_W_Mo	-0.387	0.308
Rh_Os_Al	-0.464	-1.540	Al_Mo_W	-0.388	0.309
Pt_Ag_Si	-0.489	-1.537	Al_W_Re	-0.258	0.312
Pd_Rh_Ge	-0.413	-1.537	Pt_Au_Re	-0.271	0.314
Ni_Al_Co	-0.347	-1.533	Ir_Ni_Co	-0.482	0.318
Ni_Co_Al	-0.347	-1.532	Cu_Ti_Pb	-0.374	0.319
Pd_Zn_Pd	-0.430	-1.511	Al_W_Ga	-0.243	0.323
Rh_Ni_As	-0.217	-1.496	Au_Cu_Ti	-0.179	0.325
Rh_In_Co	-0.348	-1.491	Cu_Rh_Pd	-0.467	0.326
Pd_Cr_Zn	-0.283	-1.488	Al_W_Cu	-0.317	0.341
Pd_Zn_Cr	-0.283	-1.488	Cu_Zn_Ti	-0.305	0.341
Rh_Mo_Zn	-0.395	-1.487	Al_W_Pb	-0.325	0.345
Ir_Pt_In	-0.228	-1.487	Rh_Ag_Ru	-0.459	0.368
Rh_Zn_Mo	-0.395	-1.487	Ni_Rh_Mo	-0.517	0.371
Rh_W_Zn	-0.405	-1.483	Ni_Ru_Pd	-0.467	0.374
Ir_Al_Ru	-0.346	-1.471	Rh_Ru_Ir	-0.484	0.374
Pt_Mo_V	-0.462	-1.448	Pd_Re_Ag	-0.337	0.388
Pt_V_Mo	-0.462	-1.448	Ag_Ag_Pt	-0.403	0.392
Ir_W_Ge	-0.359	-1.443	Pt_Re_Pd	-0.427	0.412
Ni_Au_In	-0.275	-1.440	Cu_Pt_Fe	-0.316	0.413
Pd_Mn_Au	-0.275	-1.436	Cu_Fe_Pt	-0.316	0.413
Pt_Pb_Pt	-0.281	-1.432	Pt_Pt_Re	-0.371	0.416

H-G_1-G_2	E_H (eV)	E_{mix} (eV)	H-G_1-G_2	E_H (eV)	E_{mix} (eV)
Pd_Cu_Pt	-0.570	-1.430	Al_W_Zn	-0.301	0.417
Ni_Pd_In	-0.184	-1.407	Cu_Cr_Pt	-0.344	0.420
Ni_In_Pd	-0.198	-1.406	Pd_Ru_Au	-0.346	0.422
Rh_Zn_Au	-0.193	-1.405	Pd_Au_Ru	-0.345	0.422
Rh_Au_Zn	-0.201	-1.401	Cu_As_V	-0.470	0.429
Pt_Ni_Ga	-0.373	-1.386	Rh_Os_Ir	-0.419	0.465
Ni_Cu_Ti	-0.472	-1.379	Ni_Au_Re	-0.359	0.467
Ni_Ti_Cu	-0.473	-1.378	Ni_Re_Au	-0.361	0.468
Ir_Si_Cr	-0.476	-1.376	Al_W_V	-0.516	0.477
Ir_Mo_Pb	-0.277	-1.365	Rh_Co_Ru	-0.358	0.490
Pt_Au_Zn	-0.307	-1.363	Cu_Al_Ru	-0.527	0.498
Ir_W_V	-0.563	-1.347	Rh_Ag_Os	-0.464	0.501
Pt_Zn_Ag	-0.455	-1.346	Cu_V_Ga	-0.195	0.507
Pt_Co_Ga	-0.481	-1.344	Ni_Au_Os	-0.390	0.537
Cu_Sb_Pd	-0.178	-1.321	Ni_Os_Au	-0.390	0.538
Al_Ti_Ni	-0.247	-1.321	Ir_Os_Ru	-0.492	0.538
Ni_Cr_Sb	-0.555	-1.313	Ni_Pd_Re	-0.476	0.549
Ni_Mn_Pb	-0.465	-1.305	Ni_Cr_Ag	-0.463	0.553
Ni_Pb_Au	-0.243	-1.301	Cu_Rh_Cu	-0.557	0.560
Rh_As_Ir	-0.522	-1.300	Ir_Ag_Ag	-0.344	0.582
Ni_Pd_Pb	-0.379	-1.298	Cu_Cr_Zn	-0.188	0.589
Ni_Si_Ru	-0.552	-1.295	Pt_Os_Mo	-0.474	0.599
Rh_Ge_Ru	-0.532	-1.285	Au_Ag_Pt	-0.458	0.600
Ir_W_Pb	-0.252	-1.279	Pt_W_Os	-0.445	0.600
Ir_Sn_Au	-0.380	-1.279	Au_Cu_Pd	-0.367	0.603
Ir_Au_Sn	-0.382	-1.278	Cu_Ni_Ti	-0.495	0.620
Ir_In_Re	-0.262	-1.267	Ag_Cu_Pd	-0.298	0.628
Ir_Zn_Zn	-0.297	-1.254	Al_W_Si	-0.194	0.635
Ni_Fe_Ti	-0.546	-1.252	Ni_Ag_Mo	-0.477	0.651
Ir_Si_Pd	-0.332	-1.231	Ag_Rh_Al	-0.339	0.662
Ir_Zn_Mo	-0.457	-1.224	Cu_Co_Zn	-0.493	0.664
Ni_Al_Cr	-0.431	-1.216	Al_Cr_W	-0.455	0.668
Ni_Mo_As	-0.553	-1.214	Pd_Ru_Ag	-0.441	0.676
Ir_V_Au	-0.386	-1.204	Pd_Fe_Au	-0.398	0.687
Ir_Si_Fe	-0.488	-1.194	Pt_Ru_Ag	-0.451	0.689
Rh_Os_Ge	-0.479	-1.152	Au_Au_Pt	-0.403	0.690
Ni_Zn_Pd	-0.244	-1.151	Ni_Re_Ir	-0.430	0.703
Ir_Au_In	-0.386	-1.144	Cu_Cr_Pd	-0.365	0.707
Ir_Rh_Si	-0.359	-1.131	Cu_Cu_Ti	-0.440	0.713
Ir_V_Ir	-0.543	-1.130	Cu_Ti_Cu	-0.439	0.713
Ir_Ni_Ga	-0.353	-1.128	Pt_Re_Ni	-0.446	0.724
Rh_Ru_As	-0.526	-1.127	Cu_Co_Pt	-0.474	0.729
Ni_In_Ni	-0.545	-1.123	Cu_Pt_Co	-0.475	0.730

H-G_1-G_2	E_H (eV)	E_{mix} (eV)	H-G_1-G_2	E_H (eV)	E_{mix} (eV)
Ni_Cr_Ga	-0.347	-1.121	Ni_Cu_Re	-0.556	0.740
Al_Mo_Au	-0.212	-1.117	Cu_In_V	-0.211	0.765
Al_W_Pd	-0.303	-1.109	Au_Co_Ti	-0.212	0.774
Ni_Cu_Pb	-0.414	-1.108	Au_Cr_Ti	-0.346	0.782
Cu_Pt_Zn	-0.243	-1.108	Cu_Ru_Ti	-0.282	0.785
Ni_Ge_Mo	-0.567	-1.100	Cu_Au_Co	-0.409	0.813
Ir_Ga_Cu	-0.456	-1.097	Cu_Co_Au	-0.409	0.813
Ni_Al_Ru	-0.397	-1.090	Pd_Ru_Pt	-0.566	0.836
Ir_Mo_As	-0.355	-1.088	Cu_Pd_V	-0.336	0.868
Ni_Pt_Pt	-0.265	-1.081	Au_Pd_Cr	-0.346	0.884
Rh_W_Pt	-0.430	-1.078	Pd_Cr_Mn	-0.544	0.885
Pt_Re_Ga	-0.234	-1.077	Pd_Mn_Cr	-0.545	0.886
Ir_Au_Si	-0.454	-1.072	Pd_Os_Au	-0.477	0.895
Rh_Zn_Cu	-0.332	-1.072	Pt_Re_Re	-0.360	0.909
Ni_Ru_Sb	-0.469	-1.062	Ni_Mo_Ru	-0.532	0.951
Pd_Au_Au	-0.192	-1.050	Ag_Ni_Au	-0.247	0.967
Cu_As_Pd	-0.175	-1.047	Pd_Re_Rh	-0.449	0.990
Ni_Al_Mo	-0.431	-1.039	Au_Mn_Cr	-0.222	1.003
Ni_Mo_Al	-0.431	-1.039	Au_V_Pd	-0.264	1.005
Pd_Re_Pb	-0.357	-1.033	Au_Cu_Cr	-0.188	1.015
Ni_In_Co	-0.475	-1.024	Pd_Cu_Fe	-0.530	1.021
Pt_Mn_Cu	-0.462	-1.022	Pd_Os_Mo	-0.559	1.052
Ni_Ge_Ru	-0.525	-1.022	Pt_Re_Ru	-0.395	1.109
Rh_Ag_Zn	-0.220	-1.019	Cu_Cr_Ag	-0.225	1.119
Rh_Zn_Rh	-0.448	-1.016	Cu_Fe_Cu	-0.425	1.139
Ir_Pt_Zn	-0.326	-1.008	Ni_Mo_Os	-0.552	1.139
Rh_Mn_Au	-0.290	-0.998	Ni_Os_Mo	-0.553	1.139
Pd_Cr_V	-0.458	-0.993	Cu_Fe_Rh	-0.472	1.197
Pt_Mn_Pd	-0.523	-0.991	Cu_Mn_Mn	-0.513	1.209
Rh_Zn_Re	-0.411	-0.990	Cu_Cr_Rh	-0.476	1.244
Ir_Si_Cu	-0.499	-0.977	Cu_Fe_Ni	-0.487	1.286
Ni_Sn_Mo	-0.513	-0.976	Ag_Al_Ti	-0.304	1.320
Cu_Pb_Pt	-0.306	-0.975	Cu_Co_Ag	-0.544	1.353
Pt_Al_Os	-0.313	-0.969	Cu_Ag_Co	-0.544	1.354
Pt_Os_Al	-0.312	-0.969	Cu_Ni_Cr	-0.568	1.357
Ir_V_Re	-0.565	-0.962	Au_Au_Rh	-0.427	1.367
Pd_Zn_Rh	-0.446	-0.961	Ag_Zn_Ti	-0.220	1.382
Pd_W_V	-0.411	-0.955	Ni_Ru_Os	-0.514	1.412
Rh_Zn_Ir	-0.530	-0.932	Ag_Pd_Cr	-0.357	1.413
Ir_Si_Ir	-0.344	-0.932	Au_Cu_Fe	-0.175	1.437
Ni_Pb_Ir	-0.412	-0.920	Cu_V_Ag	-0.322	1.464
Rh_Au_Mo	-0.319	-0.911	Cu_Cr_Ir	-0.544	1.508
Rh_Mo_Au	-0.319	-0.911	Pt_Ru_Ru	-0.509	1.539

H-G_1-G_2	E_H (eV)	E_{mix} (eV)	H-G_1-G_2	E_H (eV)	E_{mix} (eV)
Rh_Au_W	-0.300	-0.907	Ni_Os_Os	-0.457	1.558
Rh_Zn_Ni	-0.450	-0.901	Au_Co_Pd	-0.349	1.572
Ir_Si_Co	-0.465	-0.892	Cu_Mo_Sn	-0.536	1.579
Pd_W_Au	-0.177	-0.885	Au_Mo_Al	-0.243	1.658
Pd_Au_Ag	-0.240	-0.877	Au_Sn_Mo	-0.178	1.667
Ir_W_Mn	-0.542	-0.844	Au_Mo_Sn	-0.207	1.667
Ir_Ge_Au	-0.426	-0.840	Ag_Ni_Cu	-0.450	1.683
Ir_Au_Ge	-0.426	-0.840	Pd_Os_Re	-0.429	1.725
Ir_Si_Ru	-0.335	-0.830	Cu_Fe_Fe	-0.534	1.754
Ni_As_Re	-0.546	-0.826	Ag_Al_Co	-0.442	1.780
Al_Ti_Mo	-0.518	-0.823	Cu_Cr_Mn	-0.558	1.814
Rh_Au_Pt	-0.329	-0.813	Cu_Mn_Cr	-0.558	1.814
Ni_Mn_Au	-0.199	-0.803	Pt_Ru_Os	-0.423	1.828
Ni_Al_Re	-0.456	-0.792	Au_Pt_Co	-0.394	1.864
Cu_Rh_Al	-0.333	-0.790	Au_Co_Pt	-0.394	1.864
Pd_Ru_As	-0.262	-0.786	Ag_Cu_Ti	-0.379	1.878
Ir_Zn_Pd	-0.372	-0.784	Cu_Rh_Ru	-0.483	1.976
Ni_Pd_Pt	-0.327	-0.778	Au_Mo_Zn	-0.213	2.022
Ni_Pt_Pd	-0.327	-0.777	Cu_Zn_Mo	-0.418	2.057
Ir_W_Mo	-0.547	-0.770	Cu_Mo_Au	-0.273	2.095
Al_Ti_Fe	-0.175	-0.762	Cu_Au_Mo	-0.272	2.095
Pd_Cu_Au	-0.326	-0.759	Pt_Os_Os	-0.344	2.120
Al_Mn_Ti	-0.433	-0.755	Ag_Ru_Al	-0.495	2.140
Cu_Au_Pt	-0.228	-0.751	Ag_Al_Ru	-0.494	2.141
Rh_W_Pd	-0.502	-0.747	Ag_Co_Ti	-0.349	2.153
Pd_Mo_Au	-0.229	-0.746	Cu_W_Pt	-0.290	2.158
Ni_Zn_Co	-0.311	-0.745	Au_Co_Fe	-0.272	2.191
Ni_Co_Zn	-0.311	-0.745	Cu_Cr_Ru	-0.461	2.260
Al_Ti_Cu	-0.242	-0.744	Cu_Fe_Ru	-0.555	2.279
Ir_Fe_Zn	-0.396	-0.736	Au_Ge_Mo	-0.267	2.311
Cu_Rh_Ga	-0.499	-0.728	Au_Mo_Ge	-0.268	2.312
Pt_Mo_Cr	-0.467	-0.727	Au_Ag_Mo	-0.262	2.366
Pd_Au_Mo	-0.249	-0.727	Au_Mo_Ag	-0.264	2.367
Rh_Mo_Pd	-0.524	-0.726	Au_Ru_Au	-0.278	2.398
Cu_Pt_Pt	-0.378	-0.717	Au_Mo_Pd	-0.328	2.426
Pt_Mo_Au	-0.304	-0.702	Cu_Mo_Ir	-0.384	2.427
Rh_Au_Cr	-0.320	-0.692	Cu_Re_Pd	-0.503	2.502
Pd_Ag_Ag	-0.252	-0.689	Ag_Zn_Ru	-0.532	2.531
Ir_Zn_Ir	-0.339	-0.689	Au_Mo_Pt	-0.323	2.559
Ir_Zn_Au	-0.177	-0.687	Ag_Au_Ru	-0.399	2.580
Ir_Au_Zn	-0.177	-0.687	Cu_W_Au	-0.489	2.611
Ir_Pt_Pt	-0.369	-0.679	Cu_W_Rh	-0.371	2.631
Ir_Ge_Ru	-0.314	-0.674	Ag_Sb_Mo	-0.400	2.661

H-G$_1$-G$_2$	**E$_H$ (eV)**	**E$_{mix}$ (eV)**	**H-G$_1$-G$_2$**	**E$_H$ (eV)**	**E$_{mix}$ (eV)**
Ni_Pd_Mn	-0.402	-0.669	Ag_Mo_Sb	-0.401	2.661
Pt_W_Mo	-0.420	-0.668	Cu_W_Zn	-0.525	2.663
Pt_Ag_W	-0.351	-0.658	Au_Cu_Mo	-0.337	2.710
Ni_V_Pd	-0.451	-0.654	Au_Mo_Cu	-0.338	2.711
Pt_Cr_Au	-0.356	-0.651	Cu_Rh_Re	-0.438	2.732
Ni_Fe_Au	-0.182	-0.638	Cu_Cr_Os	-0.545	2.766
Ni_Co_Pt	-0.341	-0.622	Ag_In_Mo	-0.331	2.769
Ir_Mo_Au	-0.387	-0.613	Au_Cr_Mo	-0.422	2.781
Pd_V_Rh	-0.549	-0.612	Cu_Ru_Ru	-0.432	2.863
Pt_Mo_Ag	-0.396	-0.604	Cu_Co_Mo	-0.440	2.883
Pd_Zn_Ir	-0.569	-0.600	Ag_Pb_Mo	-0.263	2.936
Ni_Au_Pd	-0.176	-0.595	Ag_Mo_Pb	-0.400	2.936
Ni_Pd_Au	-0.177	-0.593	Au_W_Zn	-0.322	2.986
Pt_Mo_Pd	-0.475	-0.588	Au_Ru_Fe	-0.402	2.991
Ir_W_Ir	-0.422	-0.587	Ag_Fe_Fe	-0.412	3.018
Ir_Mn_Au	-0.348	-0.585	Ag_V_Ru	-0.287	3.026
Pd_Au_Pt	-0.473	-0.582	Ag_Mo_Al	-0.362	3.072
Pd_Pt_Au	-0.476	-0.582	Au_Mo_Ni	-0.434	3.123
Rh_Au_Pd	-0.312	-0.573	Ag_Zn_Mo	-0.291	3.174
Rh_Cu_Mo	-0.532	-0.572	Cu_Cr_Re	-0.547	3.178
Pt_Cu_Mo	-0.425	-0.572	Cu_Re_Co	-0.477	3.229
Pt_Mn_Co	-0.475	-0.569	Au_W_Pt	-0.263	3.239
Ni_Mo_In	-0.542	-0.561	Au_Co_Ru	-0.379	3.288
Ni_Rh_Pt	-0.360	-0.554	Cu_Co_W	-0.531	3.290
Pd_Pd_Au	-0.421	-0.547	Ag_Mo_Ag	-0.312	3.294
Pd_Au_Pd	-0.419	-0.547	Cu_Fe_W	-0.521	3.349
Pt_Fe_Au	-0.328	-0.539	Au_Mo_Ir	-0.299	3.351
Ni_Fe_Pd	-0.358	-0.524	Au_W_Si	-0.522	3.386
Ni_Pd_Fe	-0.360	-0.524	Au_Au_Re	-0.347	3.478
Rh_Zn_Os	-0.459	-0.522	Au_Mo_Co	-0.508	3.487
Cu_Pt_Pd	-0.420	-0.522	Au_Ag_Re	-0.463	3.502
Rh_Os_Zn	-0.460	-0.521	Ag_Mo_Si	-0.432	3.502
Ir_Zn_Cu	-0.368	-0.517	Au_Re_Pd	-0.506	3.557
Ni_Mn_Cu	-0.385	-0.512	Cu_Mo_Re	-0.468	3.564
Ir_Pt_Fe	-0.435	-0.501	Au_Re_Cr	-0.461	3.574
Al_Mo_Ag	-0.196	-0.499	Au_Pt_Re	-0.391	3.708
Ni_W_In	-0.520	-0.498	Au_Cu_Re	-0.535	3.823
Rh_Cu_Au	-0.272	-0.486	Ag_Pb_W	-0.568	4.020
Pd_Mo_Ag	-0.298	-0.483	Au_Co_W	-0.538	4.079
Ir_As_Rh	-0.392	-0.470	Ag_Ag_Re	-0.563	4.339
Ir_Rh_As	-0.397	-0.469	Ag_Co_Mo	-0.516	4.499
Ir_Pt_Re	-0.367	-0.468	Au_W_Re	-0.416	4.621
Rh_Rh_Pt	-0.487	-0.467	Ag_Mn_W	-0.550	4.689

H-G$_1$-G$_2$	**E_H (eV)**	**E_{mix} (eV)**	**H-G$_1$-G$_2$**	**E_H (eV)**	**E_{mix} (eV)**
Ni_Pd_Pd	-0.353	-0.461	Ag_Cr_W	-0.384	4.713
Rh_Mo_Ag	-0.453	-0.459	Ag_Ir_Os	-0.467	5.006
Pd_Pd_Fe	-0.505	-0.458	Ag_W_Os	-0.390	5.748

References

(1) Ong, S. P. et al. Python Materials Genomics (pymatgen): A robust, open-source python library for materials analysis. *Comp. Mater. Sci.* **2013**, *68*, 314-319.

(2) Larsen, A. H. et al. The atomic simulation environment—a Python library for working with atoms. *J. Phys. Condens. Matter* **2017**, *29*, 273002.

(3) Kresse, G. & Hafner, J. Ab initio molecular-dynamics simula-tion of the liquid-metal-amorphous-semiconductor transition in germanium. *Phys. Rev., B Condens. Matter* **1994**, *49*, 14251-69.

(4) Kresse, G. & Furthmuller, J. Efficiency of ab-initio total energy calculations for metals and semiconductors using a plane-wave basis set. *Comp. Mater. Sci.* **1996**, *6*, 15-50.

(5) Chen, Y. Y.; Zhang, Y.; Zhang, X.; Tang, T.; Luo, H.; Niu, S.; Dai, Z. H.; Wan, L. J.; Hu, J. S. Self-Templated Fabrication of $MoNi_4/MoO_{3-x}$ Nanorod Arrays with Dual Active Components for Highly Efficient Hydrogen Evolution. *Adv. Mater.* **2017**, *29*, 1703311.

(6) Zhang, J.; Wang, T.; Liu, P.; Liao, Z.; Liu, S.; Zhuang, X.; Chen, M.; Zschech, E.; Feng, X. Efficient Hydrogen Production on $MoNi_4$ Electrocatalysts with Fast Water Dissociation Kinetics. *Nat. Commun.* **2017**, *8*, 15437.

(7) Du, W.; Shi, Y.; Zhou, W.; Yu, Y.; Zhang, B. Unveiling the In Situ Dissolution and Polymerization of Mo in Ni_4Mo Alloy for Promoting Hydrogen Evolution Reaction. *Angew. Chem. Int. Ed.* **2021**, *60*, 7051-7055.